https://doi.org/10.1016/j.conbuildmat.2020.120356

COMPRESSIVE BEHAVIOUR OF SLENDER FRP-CONFINED CONCRETE-ENCASED CROSS-SHAPED STEEL COLUMNS

Le Huang[a], Tao Yu[b,a*], Zhen-Yu Wang[c*] and Shi-Shun Zhang[d]

[a]*School of Civil, Mining & Environmental Engineering, Faculty of Engineering & Information Sciences, University of Wollongong, Australia.*
[b]*Department of Civil and Environmental Engineering, The Hong Kong Polytechnic University, Hung Hom, Kowloon, Hong Kong, China. Email: tao-cee.yu@polyu.edu.hk*
[c]*School of Civil Engineering, Harbin Institute of Technology, Harbin, China. Email: zhenyuwang@hit.edu.cn*
[d]*School of Civil Engineering and Mechanics, Huazhong University of Science and Technology, Wuhan, China.*

ABSTRACT

Fibre-reinforced polymer (FRP)-confined concrete-encased cross-shaped steel columns (FCCSCs) consist of a square FRP outer tube with round corners, a cross-shaped inner steel section and concrete filled in the between. The unique configuration of FCCSCs ensures that the concrete in the columns is well confined despite the square column shape, as demonstrated by the relevant existing research. The existing work on FCCSCs, however, has been limited to the behavior of short FCCSCs under axial compression. With their optimal configuration, the use of FCCSCs means that considerably reduced section dimensions may be adopted for the same load demand, leading to relatively slender columns in practice. In addition, the load eccentricity is an important parameter to consider in the column design. This paper presents the first-ever experimental study on the behaviour of slender FCCSCs. The test variables in this study included the load eccentricity, the slenderness ratio of the column and the thickness of FRP tube. The test results confirm the excellent structural performance of slender FCCSCs, and show that the load capacity of FCCSCs decreases with the slenderness ratio and the load eccentricity. Nevertheless, the confinement effects on the behavior of FCCSCs were found to be remarkable even when the column slenderness ratio and load eccentricity are large.

KEYWORDS

Fibre-reinforced polymer (FRP); Concrete; Steel section; Hybrid columns; Tubular columns; Slender columns; Eccentric compression.

1 INTRODUCTION

In the past three decades, fibre-reinforced polymer (FRP) has gained increasingly wide applications in structural engineering due to its well-known advantages such as its high strength-to-weight ratio and excellent corrosion resistance [1]. One of the most popular applications of FRP is for the strengthening of existing reinforced concrete (RC) columns [1-8]. More recently, hybrid columns incorporating an FRP confining tube as well as steel and concrete have attracted increasing research attention [9-19]. Such columns can be collectively termed hybrid FRP-concrete-steel (FCS) tubular columns [20]. FRP-confined concrete-encased cross-shaped steel columns (FCCSCs) are a new form of hybrid FCS columns recently proposed by the authors [21]. An FCCSC consists of a square FRP outer tube with round corners, a cross-shaped inner steel section and concrete filled in the between. The FRP outer tube acts as both an external confining device and an anti-corrosion protection skin, while the inner steel section acts as both longitudinal and lateral reinforcement to the concrete core. Huang et al. [21] presents the conceptual development of FCCSCs as well as an experimental study which demonstrated some structural advantages of the new column. The experimental study presented by Huang et al. [21], however, has been limited to short FCCSCs under axial compression. It is well known that most of the columns in practice are subjected to combined axial compression and bending due to load eccentricities. Additionally, the effect of column slenderness on the compressive behaviour of a column is an important issue to be addressed.

Many experimental studies have been conducted on slender FRP-confined concrete columns with (e.g. Ref [22-24]) or without steel reinforcing bars (e.g. Ref [25-27]). These studies have confirmed that FRP confinement can enhance the strength and ductility of the slender columns. It has also been reported in these studies that the increase of the load eccentricity and/or column slenderness generally leads to reduction of the load capacity of the column.

No existing experimental study has been done on slender FCCSCs. Karimi et al. [28-29] reported experimental studies on slender columns with a similar cross-sectional configuration: concrete-filled FRP tubes with a steel H-section. It was confirmed by Karimi et al. [28-29] that the tested columns have good structural performance including high loading capacity and good ductility. Karimi et al.'s studies [28-29] appear to be the only studies on slender hybrid FCS columns with an open steel section, and they did not investigate the effect of load eccentricity.

Against this background, an experimental study has recently been completed by the authors on the short-term behaviour of FCCSCs with various slenderness ratios under both concentric and eccentric compression. The detailed experimental program and the test results are presented and discussed in the following sections.

2 EXPERIMENTAL PROGRAM

2.1 Specimens

In total, 16 FCCSC specimens were prepared and tested in this study, including 12 relatively slender specimens and four short specimens for comparison. All 16 specimens had the same side length $b = 200$ mm. Steel sections of identical cross-sectional dimensions were used for all the 16 specimens, and the dimensions of the steel section were selected based on the dimensions of typical steel H sections in the relevant technical standards [e.g., 30-31] and the steel plates available in the market. Prefabricated square glass FRP tubes were used for these specimens, and they each had four round corners with a radius of 25 mm (i.e. 1/8 of the side length). The glass fibres in the FRP tubes were oriented in nearly the hoop direction of the tube to provide confinement to the concrete and steel, with the angles between the fibres and the longitudinal axis of the FRP tube being ±80 degrees. Similar FRP confining tubes have been widely used in existing studies for the same purpose [e.g., 14, 16]. The cross-sectional configuration of the specimens and its key dimensions are shown in Figure 1. The short columns all had a height of 500 mm, while three different column heights (i.e., L =1000, 1600, 2400 mm) were adopted for the 12 relatively slender specimens, lending to three different height to side length ratios (i.e., L/b = 5, 8, 12). Among the 12 specimens, three specimens had a L/b ratio of 5, six specimens had a L/b ratio of 8 and the remaining three specimens had a L/b ratio of 12. The specimens with the L/b ratio of 5 and 12 all had a 1.2 mm thick FRP tube. Among the six specimens with a L/b ratio of 8, three specimens had a 1.2 mm thick FRP tube while the other three had a 2.4 mm thick FRP tube. Therefore, the 12 relatively slender specimens can be categorized into four groups with three specimens in each group as shown in Table 1. Three different load eccentricities (i.e., 0, 35, 70 mm) were applied for the three specimens in each of the four groups, respectively; the load eccentricities at the two ends of each specimen were the same. The four short FCCSCs had the same height of $L = 500$ mm, leading to a height to side length ratio of L/b = 2.5. They included two pairs of nominally identical specimens, with FRP tube thicknesses of 1.2 mm and 2.4 mm, respectively (Table 1).

The slenderness ratio (λ) are also listed in Table 1 for all the specimens. For an FCCSC with a side length b and a corner radius r, its gross cross-sectional area A_0 and second moment of inertia I_0 can be found by Eqs. 1 and 2, respectively. The radius of gyration r_g can be calculated by Eq. 3 and then the slenderness ratio λ can be found by Eq. 4 [32].

$$A_0 = b^2 - (4 - \pi)r^2 \tag{1}$$

$$I_0 = \frac{b^4}{12} - \left[\frac{16-3\pi}{12} r^4 + (4 - \pi)(\frac{b}{2} - r)^2 r^2\right] \tag{2}$$

$$r_g = \sqrt{I_0/A_0} \tag{3}$$

$$\lambda = kL/r_g \tag{4}$$

where L is the physical column length and kL is the effective column length: for hinged-hinged supported columns $k = 1$ and for fixed-fixed supported columns $k = 0.5$ [32]. It should be pointed out that the calculation of λ based on Eqs. 1, 2, 3 and 4 does not account for the effect of the steel section in the FCCSC. When accounting for the effect of the steel section, the so-called transformed cross-sectional area A_t, transformed second moment of inertia I_t , transformed radius of gyration r_{gt} and the resulting transformed slenderness ratio λ_t can be calculated by Eqs. 5, 6, 7 and 8, respectively, as follows [24]:

$$A_t = A_0 + (n_e - 1)A_s \tag{5}$$

$$I_t = I_0 + (n_e - 1)I_s \tag{6}$$

$$r_{gt} = \sqrt{I_t/A_t} \tag{7}$$

$$\lambda_t = kL/r_{gt} \tag{8}$$

where A_s and I_s are the cross-sectional area and the second moment of inertia of the steel section, respectively; n_e is the ratio between the elastic modulus of the steel and that of the concrete in FCCSCs.

According to the above equations, for an FCCSC with given values of side length b and effective length kL, the value of the corner radius r has little effect on the slenderness ratio of the FCCSC. In addition, it is found that the steel section in FCCSCs has only marginal effects on the calculated slenderness ratio of the FCCSCs. For the specimens in the current study, the value of λ_t calculated form Eq. 8 is smaller than the value of λ calculated from Eq. 4 by only around 2.0%. The slenderness ratios calculated from Eq. 4 are thus simply used in the present study as listed in Table 1.

For convenience of reference, each of the test specimens was given a name: the name starts with the capital letter 'F' which refers to FCCSC, followed by a number (i.e., 2.5. 5, 8 or 12) which indicates the height to side length ratio (L/b) of the specimen. Following the number is another Capital letter 'A' or 'B', denoting the FRP tube thickness (A for 1.2 mm and B for 2.4

mm). For the relatively slender FCCSC specimens, the name then ends with another number (i.e., 0, 35 or 70) which refers to the load eccentricity applied to the specimen. For the short FCCSC specimens, the name ends with a Roman numeral (i.e., I or II) to differentiate the two nominally identical specimens of each pair. For example, F-8-A35 refers to the FCCSC specimen of which the height to side length ratio is L/b =8, confined by the FRP tube of 1.2 mm thickness and was subjected to 35 mm load eccentricity; F-2.5-B-I refers to the first short FCCSC specimen with the height to side length ratio of L/b =2.5 and the FRP tube of 2.4 mm thickness. Table 1 summarizes the key information of the specimens.

2.2 Material Properties

The relatively slender FCCSC specimens and the short FCCSC specimens were prepared with two different batches of ready-mixed concrete of the same target strength. Standard plain concrete cylinders (150 mm × 300 mm) were prepared and tested to obtain the mechanical properties of each batch of concrete. Based on compression tests of these concrete cylinders according to Ref [33], the average cylinder strength of the concrete in the test period was 32.2 MPa for the relatively slender specimens and 32.8 MPa for the short specimens. For the concrete used for the four short FCCSC specimens, the axial strain at the peak stress was measured to be 0.0024. For the relatively slender specimens, the axial strain at the peak stress of the concrete was not measured due to an equipment problem, but it can be expected to be similar to that of the short specimens. The obtained concrete properties are summarized in Table 2.

The cross-shaped steel sections in the present study were made from rectangular steel plates of the required dimensions by welding. The rectangular steel plates were cut from large pieces of steel sheets of the required thicknesses (i.e., 3.2 mm and 4.5 mm). For each of the two types of steel plates, two steel coupons were cut from the cross-shaped steel sections in the longitudinal direction, and tensile tests were conducted on the steel coupons according to Ref [34]. According to the coupon test results, the steel plates with the thicknesses of 3.2 mm and 4.5 mm had yield stresses of 290 MPa and 284 MPa, respectively, while had ultimate stresses of 400.5 MPa and 403 MPa, respectively, as listed in Table 2.

The square FRP tubes were fabricated by a filament-winding process using a mould which was specifically designed for this project. Three FRP coupons were cut from each type of FRP tube in the hoop direction, and tensile tests were conducted on these FRP coupons according to Ref [35]. According to the coupon test results, for both the thin FRP tube (1.2 mm thickness) and the thick FRP tube (2.4mm thickness), the elastic modulus was 26.8 GPa as listed in Table 2.

2.3 Preparation of Specimens

To facilitate the connection between the steel section and the hinge supports, additional cross-shaped steel plates (15.0 mm thickness) with six threaded holes (see Figure 2) were first welded to each of the ends of the each cross-shaped steel sections with good alignment. The steel sections and the FRP tubes were then vertically fixed in a formwork with the steel sections being placed inside the corresponding FRP tubes. The seams between the bottoms of the FRP tubes and the baseboard were sealed with silicone gel to avoid water leakage. Concrete was then cast for all the specimens with proper vibration. The threaded holes of the steel plates (Figure 2) were well protected during the casting to avoid being filled with concrete. The specimens were cured at ambient temperature until the test date. Figure 3 shows the specimens in preparation.

2.4 Test Setup and Instrumentation

The relatively slender specimens were tested under concentric or eccentric compression and the four short specimens were all tested under concentric compression. During the test, two steel hinge supports were used for each relatively slender specimen, while the short specimens were tested with the column ends in direct contact with the loading plates of the test machine, which is the same as most previous tests [21].

The photos of the steel hinge support are shown in Figure 4. The hinge support consists of two parts: the cup-shaped part (see Figure 4a and 4b) with a round groove (or two round grooves) at its bottom and the wedge-shaped (see Figure 4c) part with a cylindrical edge. The cylindrical edge of the wedge-shaped part and the round groove(s) of the cup-shaped part were designed to closely and smoothly fit each other to form the hinge support. Before the test, the two ends of the specimen were first concentrically fit into the cup-shaped parts of the two hinge supports. Bolts were then used to tie the cup-shaped parts to the steel plates (Figure 2) welded on the steel section via the predrilled holes (see Figures 4a and 4b), so that reliable transmission of tensile forces can be ensured between the steel section and cup-shaped parts. In addition, several bolts were also used on the sidewalls of the cup-shaped parts (see Figure 4a) to further ensure that the cup-shaped parts were tightly connected to the specimen. The load eccentricity (e) applied on the specimen was determined by the relative position of the round groove on the cup-shaped part of the hinge support as shown in Figure 4d. With the cup-shaped parts properly mounted on the specimen, the specimen was then installed in the test machine with the cylindrical edges of the wedge-shaped parts fitted into the round grooves of the cup-shaped parts.

Figure 5 shows the layout of strain gauges on the cross-shaped steel section and those attached on the FRP tube at the mid-height of the FCCSC specimens. For each relatively slender specimen, eight axial strain gauges of 10 mm gauge length were attached on the steel section to measure the axial strains at different locations, while four axial strain gauges and eight lateral strain gauges of 20 mm gauge length were applied on the FRP tube to measure the axial and hoop strains at different locations (see Figure 5a). For each short specimen, two axial strain gauges and two lateral strain gauges of 10 mm gauge length were attached on the webs of the steel section to measure the axial and lateral strains, while eight lateral strain gauges of 20 mm gauge length were used to measure the hoop strains of the FRP tube at the round corners and the middle of the flat sides (see Figure 5b).

Figures 6 shows the test setups. Seven linear variable displacement transducers (LVDTs) were used for each relatively slender specimen as shown in Figure 6(a): two LVDTs (L1 and L2) were used to measure the total shortening of the distance between the two loading plates of the test machine; one LVDT (L3) was used to measure the lateral deflection of the specimen at the mid-height; the other four LVDTs (L4, L5, L6 and L7) were used to measure the average curvature in the 200 mm mid-height region of the specimen. L4 and L5 were used to measure the average compressive strain ε_c^{avg} on the compressive side of the specimen while L6 and L7 were used to measure the average tensile strain ε_t^{avg} on the tensile side. The lateral distance between the two pairs of LVDTs was $D = 550$ mm, and the average curvature can be obtained as $\left|\varepsilon_c^{avg} - \varepsilon_t^{avg}\right|/D$. For short FCCSCs, only four LVDTs were used in the test as shown in Figure 6(b): two LVDTs were used to measure the total displacement of the specimens and the other two LVDTs were used to measure the displacement of the 150 mm mid-region of the specimens. The photos of the relatively slender FCCSC specimens and short FCCSC specimens in the test are shown in Figure 7.

3 TEST RESULTS AND DISCUSSIONS

3.1 General Test Observation and Failure Modes

The tests of the relatively slender specimens were terminated when the rupture of FRP tube occurred. For all specimens except for F-8-A0 and F-8-A70, the FRP rupture happened at around the mid-height of the specimens on the compression side; for F-8-A0 and F-8-A70, the FRP rupture prematurely happened at the end region due to local stress concentration. The typical failure modes of the relatively slender specimens of various slenderness ratio under eccentric compression ($e \neq 0$) are presented in Figure 8a. As shown in this figure, the relatively slender columns failed with large bending deformation which tended to localise in their mid-height regions, leading to the rupture of FRP tube in this region. The typical close-up photos of the rupture of FRP tubes of the relatively slender FCCSCs are presented in Figure 8b. It is shown in this figure that the rupture of the FRP tubes all occurred within the flat side on the compression side. The typical failure modes of the short FCCSCs under concentric compression are presented in Figure 9. As shown in this figure, failures of the short specimens were marked by rupture of the FRP outer tube within the flat side at around the mid-height of the specimen, which was similar to the test observations presented in Ref [21].

The FRP tubes of the relatively slender specimens were removed at the rupture position to inspect the deformation of the steel sections, and the typical photos are shown in Figure 10. As presented in this figure, slight local buckling, in the form of small ripples bent outward, was found on the flange of the steel section on the compression side of the specimens. The slight local buckling is believed to occur close to or at the rupture of FRP tube.

3.2 Axial Load-Displacement Behaviour

The axial load-displacement curves and axial load-axial strain curves of the four short specimens are shown in Figure 11. Figures 12-14 show the axial load-displacement curves of the relatively slender specimens. The axial strains in Figure 11b were calculated using the readings of the LVDTs mounted at the mid-height region of the specimens (see Figure 6), while the axial displacement shown in Figure 11-14 were the shortenings of the distance between the two loading points at the column ends, which were measured by two LVDTs (see Figure 6). It should be noted that for the eccentrically loaded relatively slender specimens, the loading points were not the geometric centres of the end sections, so the axial displacement shown in the figures included that caused by the rotation of the end sections and is typically larger than the axial displacement between the geometric centres of the two end sections.

As can be seen in Figure 11a, the short FCCSC specimens all have approximately bilinear axial load-displacement curves and axial load-axial strain curves. The curves are all terminated at the rupture of the FRP tube. As listed in Table 3, the average ultimate axial load of the two identical short specimens F-2.5-A-I and F-2.5-A-II is 2374 kN, while that of F-2.5-B-I and F-2.5-B-II is higher (i.e. 2820 kN) as their FRP outer tubes were thicker and thus the concrete core was better confined. As further indicated in Figure 11b, the average ultimate axial strain of F-2.5-A-I and F-2.5-A-II is 0.018 while that of F-2.5-B-I and F-2.5-B-II reaches 0.031.

Before making further discussions on the relatively slender specimens, it should be pointed out that two of the specimens (i.e., F-8-A0 and F-8-A70) failed prematurely at the end region, which could have somehow affected their behaviour, especially their ultimate state. The test results of these two specimens are still presented in the relevant figures as references, but their premature failure mode is given due consideration in making the conclusions.

The comparisons in Figures 12 show the effect of slenderness ratio on the axial load-displacement curves of the relatively slender specimens. It is apparent in Figure 12 that the initial stiffness of the curves generally decreases with the slenderness ratio for the eccentrically-loaded specimens. With the increase of axial load and thus the lateral deflection, the stiffness of the specimens started to decrease and such decrease appears to be quicker for longer specimens (e.g. Figure 12c) which had a larger lateral deflection at the same axial load. Figure 12 also shows that the increase of slenderness ratio resulted in substantial reduction in the ultimate axial loads of the specimens. This is because a larger slenderness ratio resulted in a larger second order moment acting on the specimen at the ultimate state.

The effect of slenderness ratio on the ultimate axial load of the specimens is further illustrated in Figure 15. As shown in Figure 15 and listed in Tables 3 and 4, when the loading eccentricity is zero ($e = 0$), the increase of slenderness ratio from 4.35 (F-2.5-A-I, II) to 17.4 (F-5-A0) resulted in only a slight decrease (3.7%) of ultimate axial load while further increase of slenderness ratio results in relatively large decreases of ultimate axial load (e.g. the increase of slenderness ratio from 17.4 to 27.9 led to a reduction of 14.2% in the ultimate axial load). In the existing studies (e.g. [37]), a threshold of slenderness ratio (i.e. slenderness limit) is generally defined for slender columns, of which the slenderness effect on the load capacity cannot be ignored (e.g. >5% as specified in Ref [37]). Based on the definition of Ref [37], the specimens of Groups F-8 and F-12 can be categorized as slender columns.

Figure 13 illustrates the effect of load eccentricity on the axial load-displacement behaviour of the relatively slender specimens. It is clearly seen in this figure that the increase of load eccentricity led to a decrease of the initial stiffness of the axial load-displacement curves. This is because the increase of load eccentricity magnifies the bending moment acting on the specimen even at the initial stage. For the same reason, the increase of load eccentricity also led to decrease in the ultimate axial load, as shown in Figure 13 and further illustrated in Figure 16. Although there are only three data points for each slenderness ratio, it can be seen in Figure 16 that the ultimate axial load decreases significantly with the load eccentricity.

Figure 14 shows the effect of FRP tube thickness on the axial load-displacement behaviour of the specimens. It can be seen that the increase of FRP tube thickness can obviously increase the ultimate axial load of the specimens and similar observation can be made in Figure 16 as well. The difference between the peak loads of F-8-A0 and F-8-B0 is 190 kN as shown in Figure 16(a). It is obvious that this difference should not have been larger than 190 kN if F-8-A0 had not failed prematurely. For the corresponding short specimens F-2.5-A-I, II and F-2.5-B-I, II, however, the difference between the ultimate axial loads is around 450 kN (see Table 3), which is much larger than 190 kN. This observation thus indicates that the effect of FRP outer tube thickness on the ultimate axial load appears to be more pronounced for specimens having a smaller slenderness ratio.

3.3 Axial Load-Lateral Deflection Behaviour

The axial load-lateral deflection curves of all the relatively slender specimens are shown in Figures 17-19. The lateral deflection of the specimens plotted in these figures was recorded by an LVDT (i.e. L3 in Figure 6a) at the mid-height of the specimens.

Figure 17 shows the effect of slenderness ratio on the axial load-lateral deflection curves of the specimens. It should be pointed out that the curves of F-8-A0 and F-8-A70 in Figure 17 are somewhat abnormal at the late stage of loading due to their premature failure at the end region. Nevertheless, it is evident from Figure 17 that the increase of slenderness ratio generally led to a decrease in the ultimate axial load and an increase in the lateral deflection at the ultimate state.

For the specimens loaded concentrically [i.e. e = 0, see Figure 17(a)], the lateral deflection was nearly zero until a certain load, while for the eccentrically loaded specimens [see Figure 17(c)], considerable lateral deflection occurred even at the early loading stage. The lateral deflection at the ultimate state was only about 55 mm for Specimen F-5-A70, while it reached over 150 mm for Specimen F-12-A70. Because of the rapider increase of lateral deflection for specimens with a larger slenderness ratio, especially after the load started to decrease, the curves of these specimens generally had a more gradual and longer descending branch compared with their shorter counterparts as shown in Figure 17. Similar observations were also reported in Tao et al.'s experimental study [36] and verified by Jiang and Teng's theoretical study [37], both on slender FRP-confined circular RC columns.

Figure 18 shows the effect of load eccentricity on the axial load-lateral deflection curves of the relatively slender specimens. As expected, the curves of the specimens loaded with a larger eccentricity generally have a smaller initial stiffness and a more gradual and longer descending branch which ends with a larger lateral deflection.

Figure 19 illustrates the effect of FRP tube thickness on the axial load-lateral deflection curves of the relatively slender specimens. As shown in Figure 19(a), Specimen F-8-B35 has a higher (by around 10%) ultimate axial load and a significantly larger ultimate lateral deflection (by over 50%) than Specimen F-8-A35. This is believed to be mainly due to the better confined concrete core in Specimen F-8-B35 as the fibres in the FRP tube oriented nearly in the hoop direction. Specimen F-8-A70 failed prematurely at the end region, but based on the curves shown in Figure 19(b), it is not unreasonable to expect that the FRP thickness has similar effects as discussed above for Figure 19(a). It may thus be concluded that both the load capacity and deformation capacity of FCCSCs increase with the thickness of the FRP outer tube, even when the load eccentricity and the slenderness ratio are large. The effect of FRP thickness on relatively slender FCCSCs appears to be more pronounced on their deformation capacity than for their load capacity.

The effectiveness of FRP confinement for slender columns has also been reported by Tao et al. [36] in their experimental study on FRP-confined slender circular RC columns under eccentric compression. According to Ref. [36], depending on the confinement stiffness of FRP, it may lead to an increase of 15%-40% in the ultimate load of the column, even for circular RC columns with a height-to-diameter ratio up to 20.4.

3.4 Axial Load-Moment Curves

Figures 20 and 21 show the axial load-moment curves of the mid-height section of the specimens. In the two figures, the moment is the total moment acting on the mid-height section of the specimens and consists of two parts, namely, the first order moment and second order moment. The former equals to the product of the axial load and the original load eccentricity, while the latter is the product of the axial load and the lateral deflection (recorded by the lateral LVDT) at the mid-height section. The first order moment, the second order moment and the total moment at the ultimate state of all specimens are listed in Table 5.

Figure 20 shows the effect of column slenderness on the axial load-moment curves and Figure 21 shows the effect of load eccentricity on the axial load-moment curves. It is shown in Figures 20 and 21 that the axial load-moment curves all have a linear initial segment, after which the moment tends to increase at an increasingly large rate until the ultimate axial load is approached. This is because the lateral deflection and thus the second order moment at the mid-height section are negligible in the early stage but become increasingly large afterwards. At the initial stage the total moment is approximately equal to the first order moment, which is not affected by the slenderness ratio (see Figure 20) and only dependent on the initial load eccentricity (see Figure 21).

Figure 20 shows that the increase of the column slenderness ratio resulted in a decrease in the ultimate axial load of the specimen. This is because for a given axial load, the second order moment at the mid-height section increases with the slenderness ratio because of the increasing lateral deflection. Figure 21 indicates that the increase of load eccentricity also led to a decrease in the ultimate axial load, and this is mainly due to the significant increase of the first order moment at the mid-height section.

3.5 Axial Load-Curvature and Moment-Curvature Curves

Figures 22 and 23 show the effect of slenderness ratio and that of load eccentricity, respectively, on the axial load-curvature and moment-curvature curves of the mid-height sections of the relatively slender FCCSC specimens. The curvatures presented in these two figures are the average curvature within the 200 mm mid-height region of the specimens and were calculated using the readings of the four vertical LVDTs [e.g., L4, L5, L6 and L7 in Figure 6(a)] as explained in Section 2.4. Similar to the discussions in Section 3.4, the moments presented in these two figures are the total moment (i.e. the sum of the first order and second order moment) at the mid-height section.

It can be seen in Figure 22(a) that the three curves initially almost coincide with each other, while in the late stage of loading, the axial load at a given curvature decreases significantly with the slenderness ratio. This is easy to understand as the first-order moment dominates at the initial stage, while the second-order moment becomes increasingly larger in the later stage. The three specimens shown in Figure 22(a), with the same load eccentricity, are subjected to the same first-order moment at the same axial load, while the second-order moment depends on the lateral deflection which increases with the slenderness ratio for the same axial load. By contrast, the total moment-curvature curves shown in Figure 22(b) do not seem to be significantly affected by the slenderness ratio. It is well known that the moment-curvature curve is a property of the cross-section and is only related to the axial load level for a given cross-section. Figure 22(b) suggests that the variation of axial load in the range shown in Figure 22(a) has only a small effect on the moment-curvature behaviour of the given cross-section of FCCSC. The observation from Figures 22(c) and (d) are similar to that from Figures 22(a) and (b), and the gap between the two moment-curvature curves in Figure 22(d) is believed to be due to that the difference in the axial load taken by the two specimens.

As expected, Figure 23(a) shows that the axial load at a given curvature decreases with the load eccentricity, as the first-order moment increases with the load eccentricity. Figure 23(b) shows that the ultimate curvature of Specimen F-5-A0 is nearly negligible compared to those of Specimens F-5-A35 and F-5-A70. This is because F-5-A0 was subjected to concentric compression and the axial load level on this specimen was much higher than that of the other two specimens at the same curvature. Similar observations can be seen from Figures 23(c) and (d).

3.6 Strains of the Steel Section

A number of strain gauges were attached at the mid-height of the cross-shaped steel sections in the relatively slender FCCSC specimens to monitor the axial strains at various positions as shown in Figure 5(a) (i.e., FC1, FC2, WC, WM1, WM2, WT, FT1 and FT2).

To study the distribution of axial strains of the steel section over its cross section, the (average) reading of the strain gauge(s) at a series of axial displacement levels were plotted in Figure 24 for two typical specimens (Specimens F-8-A35 and F-8-B35) up to their respective peak load. It is observed in Figure 24 that: (1) the axial strains on the steel section had an approximately linear distribution, which means the so-called ‘plane section assumption’ is generally valid; (2) the steel flanges in both the tensile side and the compressive side of the specimens already yielded before reaching the peak axial load. These observations are important for the development of theoretical models and simple design approaches for FCCSCs.

3.7 Strains of the FRP Tube

The FRP outer tubes can enhance the load capacity of FCCSCs by confining the concrete core as presented in the previous sections. To further illustrate the behaviour of the FRP tubes of relatively slender FCCSCs subjected to eccentric compression, the hoop strain behaviour of the FRP outer tubes are discussed in detail in this section. Comparisons of hoop strain-lateral deflection (at the mid-height section) curves were made to study the effects of the FRP tube thickness, load eccentricity and column slenderness on the behaviour of the FRP tubes as shown in Figures 25 -27.

For an FCCSC under eccentric compression, the hoop strains of the FRP tube on the compression side are generally much higher than that on the tension side. This is because the lateral expansion of the concrete in the compression side is much more significant. In Figures 25-27, the comparisons of hoop strain-lateral deflection curves on both the compression sides and the tension sides of the specimens are made. In these figures, the term "mid flat-side" refers to the hoop strain at the middle of the compression side (i.e., "CL" in Figure 5) or the middle of the tension side (i.e., "TL" in Figure 5); the term "corners" refers to the average hoop strain of the two corners on the compression side (i.e., "CCL1" and "CCL2" in Figure 5) or that of the two corners on the tension side (i.e., "TCL1" and "TCL2" in Figure 5).

Figure 25 illustrates the effect of FRP tube thickness on the hoop strain-curvature curve by the comparisons between F-8-A35 and F-8-B35. For the FRP hoop strain behaviour on the compression side, the following two observations can be made from Figure 25(a): (1) there is little distinction between the hoop strains at mid flat-side and those at the corners; (2) for a given lateral deflection, the increase of FRP tube thickness led to a decrease of FRP hoop strain. This is simply because a thicker FRP tube thickness can better restrain the expansion of the concrete core and improve the load capacity of the column (see Figure 19). On the other hand, Figure 25(b) shows that the variation of FRP tube thickness has a much smaller effect on the hoop strains of the FRP tube on the tension side of the specimens. This is not surprising as significant lateral expansion of concrete occurred only on the compression side.

Figure 26 shows the effect of load eccentricity on the hoop strain-lateral deflection curves by the comparisons between F-12-A35 and F-12-A70. It is clearly illustrated that at the same lateral deflection, the hoop strains of F-12-A35 were slightly larger than that of F-12-A70 on both the compression side and the tension side. This is because at the same lateral deflection, the higher axial load acting on F-12-A35 (see Figure 18d) makes the concrete core of F-12-A35 (especially on the compression side) expand more significantly.

Similar comparisons of the hoop strain-lateral deflection curves were made between F-8-A35 and F-12-A35 in Figure 27 to study the effect of the column slenderness ratio on the hoop strain behaviour of the FRP tubes of relatively slender FCCSCs. It is evident in Figure 27 that at the same lateral deflection, the hoop strain of F-8-A35 is obviously larger than that of F-12-A35. Again, this is mainly due to the fact that F-8-A35 carried a higher axial load than F-12-A35 at the same lateral deflection (see Figure 17b) and thus the expansion of the concrete core in F-8-A35 is more significant. As the same FRP tube (with the same rupture strain) was used in both specimens, this observation also explains why Specimen F-12-A35 has a larger lateral deflection than Specimen F-8-A35 at the ultimate state (Figure 17b).

4 CONCLUSIONS

This paper has provided the first insight into the compressive behaviour of slender FCCSCs through a detailed experimental study. The test variables in this experimental study included the column slenderness ratio, the load eccentricity and the FRP tube thickness. The effects of these important factors on various aspects of the column behaviour have been clarified in the paper. The following conclusions can be drawn based on the test results and discussions:

(1) The slender FCCSC specimens under eccentric compression failed by rupture of the FRP tubes on the compression side at the mid-height of the column.

(2) Even for the FCCSC specimens with a slenderness ratio of up to 27.9 ($L/b = 8$), the FRP tube still provides considerable confinement to the concrete and thus increases the load and deformation capacity of the specimens. Nevertheless, the increase of column slenderness ratio tends to reduce the effectiveness of FRP confinement for FCCSCs.

(3) The thickness of FRP tube has a considerable effect on the behaviour of slender FCCSCs, especially their deformation capacity. The increase of FRP tube thickness from 1.2 mm to 2.4 mm in this study led to an increase of around 10% in the ultimate axial load and an increase of over 50% in the ultimate lateral deflection, for FCCSC specimens with a

slenderness ratio of 27.9 and a load eccentricity of 35 mm.

(4) The load capacity of FCCSCs reduces with the slenderness ratio and the load eccentricity. However, the lateral deformation of FCCSCs at the ultimate state (i.e. FRP rupture) may increase with the slenderness or the load eccentricity. After the peak load, slender FCCSCs tend to have a more gradual descending branch of the load-lateral deformation curve, compared with their short counterparts.

(5) The deformation of the steel section in slender FCCSCs under eccentric compression generally satisfies the ‘plane section assumption’.

ACKNOWLEDGEMENTS

The authors are grateful for the financial support from the Australian Research Council through its Discovery Projects funding scheme (project ID: DP170102992) as well as that from the National Natural Science Foundation of China (Grant No. 51478143).

REFERENCES

[1] Hollaway LC, Teng JG. Strengthening and rehabilitation of civil infrastructures using fibre-reinforced polymer (FRP) composites. England: Woodhead Publishing and Maney Publishing; 2008.

[2] Wang, Z., Wang, D., Smith, S.T. and Lu, D., 2012. CFRP-confined square RC columns. I:

Experimental investigation. Journal of Composites for Construction 2012; 16(2):150-160.

[3] Mostofinejad, D. and Ilia, E. Confining of square RC columns with FRP sheets using corner strip–batten technique. Construction and Building Materials 2014; 70:269-278.

[4] Moshiri, N., Hosseini, A. and Mostofinejad, D. Strengthening of RC columns by longitudinal CFRP sheets: Effect of strengthening technique. Construction and Building Materials 2015; 79:318-325.

[5] Mostofinejad, D. and Torabian, A. Experimental study of circular RC columns strengthened with longitudinal CFRP composites under eccentric loading: comparative evaluation of EBR and EBROG methods. Journal of Composites for Construction 2016; 20(2):04015055.

[6] Saljoughian, A. and Mostofinejad, D. Grooving methods in square RC columns strengthened with longitudinal CFRP under cyclic axial compression. Engineering Structures 2018; 174:724-735.

[7] NoroozOlyaee, M. and Mostofinejad, D. Slenderness Effects in Circular RC Columns Strengthened with CFRP Sheets Using Different External Bonding Techniques. Journal of Composites for Construction 2019; 23(1):04018068.

[8] Lin, G., Zeng, J.J., Teng, J.G. and Li, L.J. Behavior of large-scale FRP-confined rectangular RC columns under eccentric compression. Engineering Structures 2020; 216:110759.

[9] Xiao, Y. Applications of FRP composites in concrete columns. Advances in Structural Engineering 2004; 7(4):335-343.

[10] Liu, X., Nanni, A. and Silva, P.F. Rehabilitation of compression steel members using FRP pipes filled with non-expansive and expansive light-weight concrete. Advances in Structural Engineering 2005; 8(2):129-142.

[11] Teng, J.G., Yu, T., Wong, Y.L. and Dong, S.L. Hybrid FRP–concrete–steel tubular columns: concept and behavior. Construction and building materials 2007; 21(4):846-854.

[12] Yu, T., Wong, Y.L. and Teng, J.G. Behavior of hybrid FRP-concrete-steel double-skin tubular columns subjected to eccentric compression. Advances in Structural Engineering 2010; 13(5):961-974.

[13] Hu, Y.M., Yu, T. and Teng, J.G. FRP-confined circular concrete-filled thin steel tubes under axial compression. Journal of Composites for Construction 2011; 15(5):850-860.

[14] Karimi, K., Tait, M.J. and El-Dakhakhni, W.W. Testing and modeling of a novel FRP-encased steel–concrete composite column. Composite Structures 2011; 93(5):1463-1473.

[15] Feng, P., Cheng, S., Bai, Y. and Ye, L. Mechanical behavior of concrete-filled square steel tube with FRP-confined concrete core subjected to axial compression. Composite Structures 2015; 123:312-324.

[16] Fanggi, B.A.L. and Ozbakkaloglu, T. Square FRP–HSC–steel composite columns: Behavior under axial compression. Engineering Structures 2015; 92:156-171.

[17] Yu, T., Teh, L.H. and Hadi, M.N.S. High strength steel plates in hybrid FRP-concrete-steel columns: concept and behavior. Advances in Structural Engineering 2017; 20(5): 797-811.

[18] Yu, T., Chan, C., Teh, L. and Teng, J.G. Hybrid FRP-concrete-steel multitube concrete columns: concept and behavior. Journal of Composites for Construction 2017; 21(6):04017044.

[19] Yu, T., Zhao, H., Ren, T. and Remennikov, A. Novel hybrid FRP tubular columns with large deformation capacity: concept and behaviour. Composite Structures 2019; 212:500-512.

[20] Yu, T. Hybrid FRP-concrete-steel tubular members. Proceedings of the 9th International Conference on FRP Composites in Civil Engineering (CICE 2018), Paris, 17-19 July, 2018.

[21] Huang, L., Yu, T., Zhang, S.S. and Wang, Z.Y. FRP-confined concrete-encased cross-shaped steel columns: concept and behaviour. Engineering Structures 2017; 152:348-358.

[22] Pan, J.L., Xu, T. and Hu, Z.J. Experimental investigation of load carrying capacity of the slender reinforced concrete columns wrapped with FRP. Construction and Building Materials 2007; 21(11):1991-1996.

[23] Fitzwilliam, J. and Bisby, L.A. Slenderness effects on circular CFRP confined reinforced concrete columns. Journal of Composites for Construction 2010; 14(3):280-288.

[24] Siddiqui, N.A., Alsayed, S.H., Al-Salloum, Y.A., Iqbal, R.A. and Abbas, H. Experimental investigation of slender circular RC columns strengthened with FRP composites. Construction and Building Materials 2014; 69:323-334.

[25] Mirmiran, A., Shahawy, M. and Beitleman, T. Slenderness limit for hybrid FRP-concrete columns. Journal of Composites for Construction 2001; 5(1):26-34.

[26] Sadeghian, P., Shekari, A.H. and Mousavi, F. Stress and strain behaviour of slender concrete columns retrofitted with CFRP composites. Journal of Reinforced Plastics and Composites 2009; 28(19):2387-2396.

[27] Vincent, T. and Ozbakkaloglu, T. Influence of slenderness on stress-strain behaviour of concrete-filled FRP tubes: Experimental study. Journal of Composites for Construction 2015; 19(1):04014029.

[28] Karimi, K., El-Dakhakhni, W.W. and Tait, M.J. Behaviour of slender steel-concrete composite columns wrapped with FRP jackets. Journal of Performance of Constructed

Facilities 2012; 26(5):590-599.

[29] Karimi, K., Tait, M.J. and El-Dakhakhni, W.W. Influence of slenderness on the behaviour of a FRP-encased steel-concrete composite column. Journal of Composites for Construction 2012; 16(1):100-109.

[30] AS/NZS 3679.1. Structural Steel Part 1: Hot-rolled bars and sections. Sydney, Australia: Standards Australia; 2016.

[31] BS 4-1. Structural Steel Sections - Part 1: Specification for Hot-Rolled Sections. London, UK: British Standards Institution; 2005.

[32] Beer, F. Statics and mechanics of materials. New York, USA: McGraw-Hill Higher Education; 2016.

[33] AS 1012.9. Methods of testing concrete-Determination of the compressive strength of concrete specimens. Sydney, Australia: Standard Australia; 2014.

[34] BS18. Method for tensile testing of metals (including aerospace materials). London, UK: British Standards Institution; 1987.

[35] ASTM D3039/D3039M. Standard test method for tensile properties of polymer matrix composite materials. Pennsylvania, USA: West Conshohocken; 2014.

[36] Tao, Z., Teng, J.G., Han, L.H. and Lam, L. Experimental behaviour of FRP-confined slender RC columns under eccentric loading. In: Advanced Polymer Composites for Structural Applications in Construction. Woodhead Publishing, 2004. P. 203-212.

[37] Jiang, T. and Teng, J.G. Theoretical model for slender FRP-confined circular RC columns, Construction and building materials 2012; 32:66-76.

Table 1. Test matrix

Specimen	Thickness of FRP tube (mm)	Column height L (mm)	Sectional Side length b (mm)	L/b	Slenderness ratio $\lambda = kL/r_g$	Load eccentricity (mm)
F-2.5-A-I	1.2	500	200	2.5	4.35 $(k = 0.5)$	0
F-2.5-A-II						
F-2.5-B-I	2.4					
F-2.5-B-II						
F-5-A0	1.2	1000	200	5	17.4 $(k = 1)$	0
F-5-A35						35
F-5-A70						70
F-8-A0	1.2	1600	200	8	27.9 $(k = 1)$	0
F-8-A35						35
F-8-A70						70
F-8-B0	2.4	1600	200	8	27.9 $(k = 1)$	0
F-8-B35						35
F-8-B70						70
F-12-A0	1.2	2400	200	12	41.8 $(k = 1)$	0
F-12-A35						35
F-12-A70						70

Table 2. Material properties

Concrete	Short FCCSCs	Compressive strength (MPa)	Axial strain at the peak stress
		32.2	0.0024
	Slender FCCSCs	32.8	N/A
Steel	3.2 mm thickness	Yield stress (MPa)	Ultimate stress (MPa)
		280.0	400.5
	4.5 mm thickness	284.0	403.0
FRP		Elastic modulus (GPa)	Ultimate tensile strain
		26.8	0.0145

Table 3 Key test results

Specimen	F_u (kN)	S_u (mm)	D_u (mm)	C_u ($10^{-3}mm^{-1}$)	$\varepsilon_{h.rup}^{avg}$
F-2.5-A-I	2327	7.9	N/A	N/A	0.0115
F-2.5-A-II	2421	9.8			0.0136
F-2.5-B-I	2783	13.3			0.0119
F-2.5-B-II	2858	15.0			0.0127
F-5-A0	2286	23.8	--	0.49	0.0092
F-5-A35	1362	7.5	9.1	0.65	0.0125
F-5-A70	901	10.0	11.7	0.60	0.0130
F-8-A0*	1963	10.6	--	--	--
F-8-A35	1136	7.6	14.4	0.30	0.0106
F-8-A70*	746	11.0	14.33	0.23	--
F-8-B0	2151	20.0	11.0	0.31	0.0040
F-8-B35	1262	7.7	14.3	0.24	0.0071
F-8-B70	806	9.0	14.0	0.33	0.0121
F-12-A0	1713	8.4	13.4	0.35	0.0093
F-12-A35	1024	6.1	18.4	0.21	0.0099
F-12-A70	664	10.6	22.2	0.19	0.0097

F_u: the ultimate axial load; S_u: the axial displacement at the ultimate axial load; D_u: the lateral deflection at ultimate axial load; C_u: the curvature at the ultimate axial load; $\varepsilon_{h.rup}^{avg}$: the average FRP hoop strain at the ultimate state.

* Specimen failed at the end regions

Table 4 Ratio between the ultimate axial load of the slender FCCSC specimens and that of the corresponding short column under concentric compression.

Specimen	$F_u/F_{u,short}$
F-5-A0	96.3%
F-5-A35	57.4%
F-5-A70	38.0%
F-8-A0*	82.7%
F-8-A35	47.9%
F-8-A70*	31.4%
F-12-A0	72.2%
F-12-A35	43.1%
F-12-A70	28.0%
F-8-B0	76.3%
F-8-B35	44.8%
F-8-B70	28.6%

F_u: the ultimate axial load; $F_{u,short}$: the ultimate axial load of the corresponding short column under concentric compression.
* Specimen failed at the end regions

Table 5 Ultimate moment of slender columns.

Specimen	First order moment (kN.m)	Second order moment (kN.m)	Total moment (kN.m)
F-5-A0	0.0	2.65	2.65
F-5-A35	41.83	30.79	72.62
F-5-A70	55.73	27.00	82.73
F-8-A0*	0.0	13.74	13.74
F-8-A35	27.26	41.93	69.19
F-8-A70*	52.16	10.68	62.84
F-8-B0	0.0	65.21	65.21
F-8-B35	27.36	57.08	84.44
F-8-B70	36.41	51.28	87.69
F-12-A0	0.0	60.24	60.24
F-12-A35	16.86	55.82	72.68
F-12-A70	27.06	41.92	68.98

* Specimen failed at the end regions

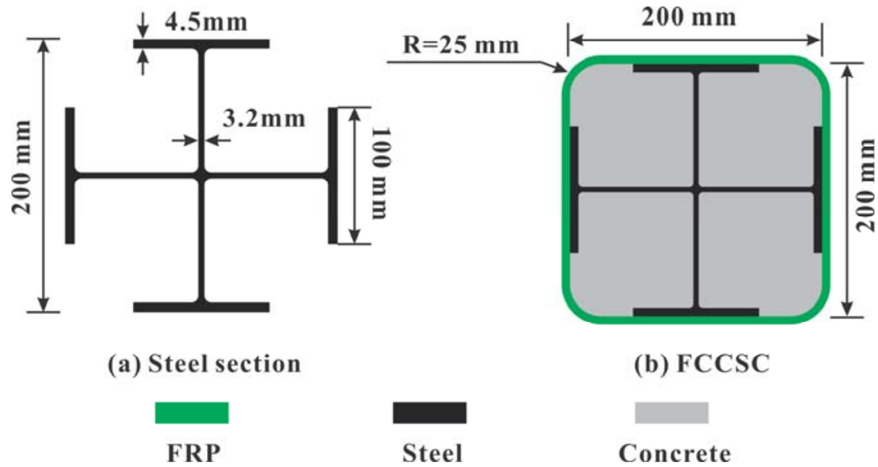

Figure 1. Cross-sectional configuration of FCCSCs

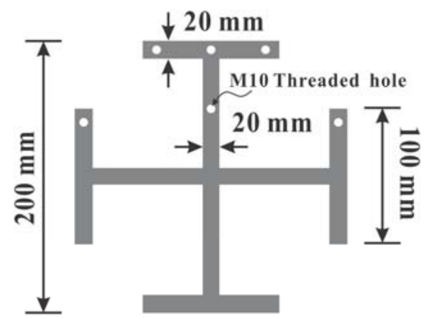

Figure 2. Cross-shaped steel plate (15 mm thickness) with threaded holes

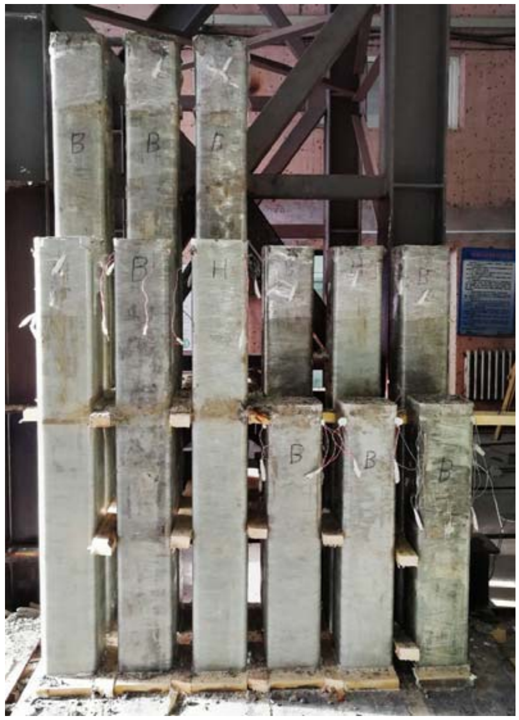

Figure 3. Specimens in preparation

(a) The cup-shaped part (seen from top)

(b) The cup-shaped part (seen from bottom)

(c) The wedge-shaped part

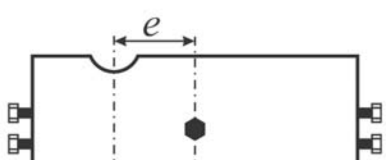

(d) Load eccentricity e

Figure 4. The cup-shaped part and the wedge-shaped part of the pinned support

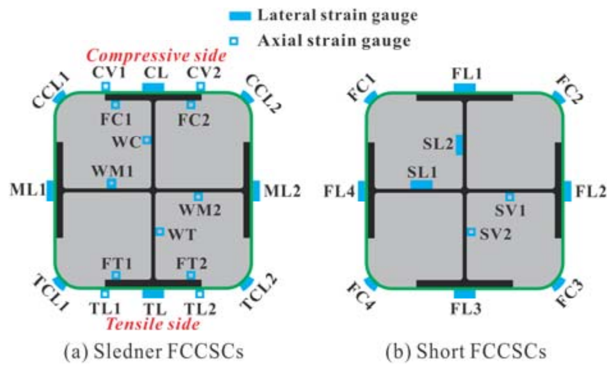

Figure 5. Layout of strain gauges on the steel section and the FRP tube of the specimens

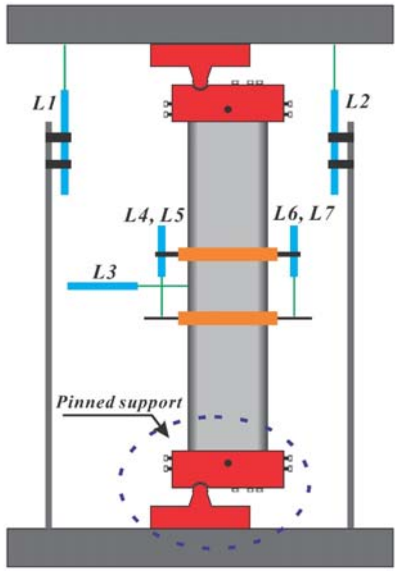

(a) Slender FCCSCs

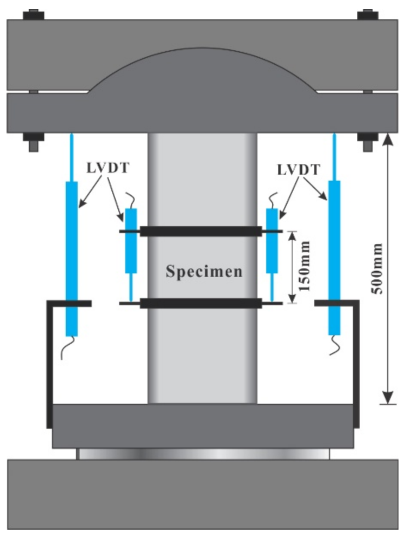

(b) Short FCCSCs
Figure 6. Schematics of the test setup and the layout of LVDTs

(a) Slender specimen

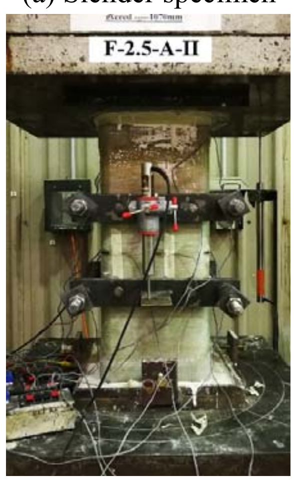

(b) Short specimen

Figure 7. Photos of specimens in test

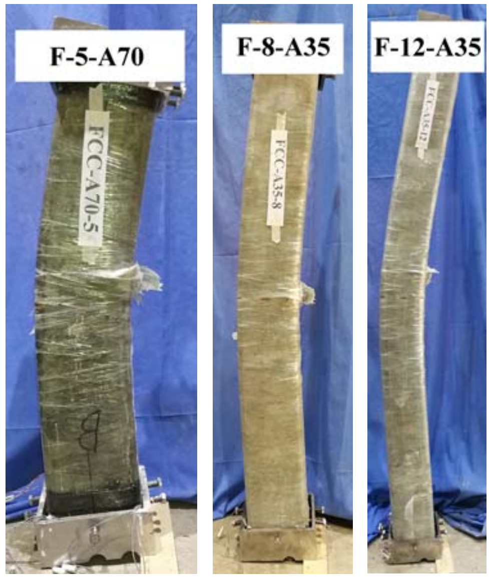

(a) Overall failure mode of slender FCCSCs

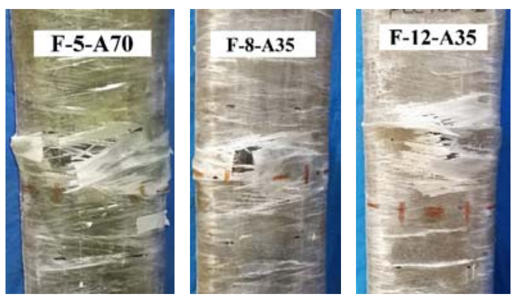

(b) Rupture of the FRP tubes of FCCSCs

Figure 8. Typical failure modes of slender FCCSCs

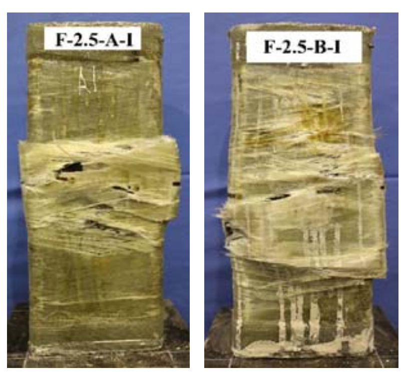

Figure 9. Typical failure modes of short FCCSCs

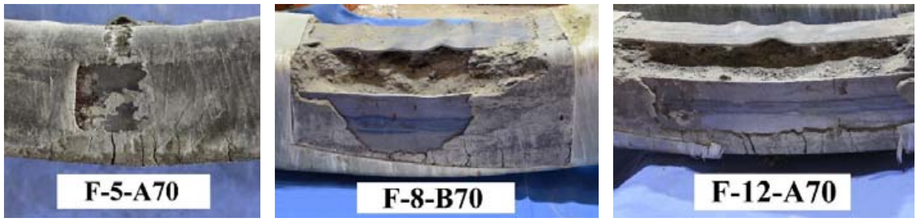

(a) (b) (c)

Figure 10. Small ripples on the steel sections at the failure of some typical specimens

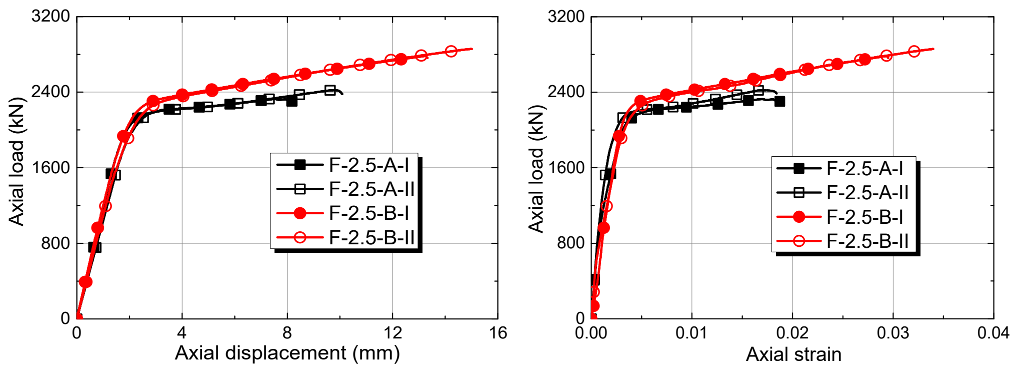

(a) Axial load-axial displacement curves (b) Axial load-axial strain curves

Figure 11. Axial load- displacement and axial load-axial strain curves of the short FCCSC specimens

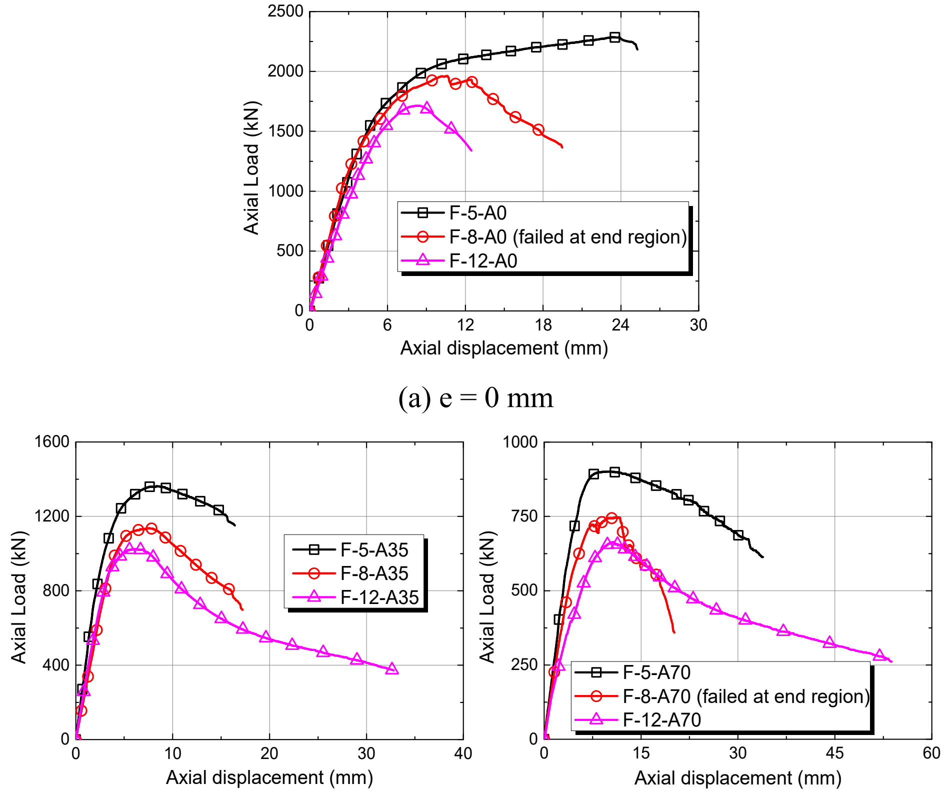

(a) e = 0 mm

(b) e = 35 mm (c) e = 70 mm

Figure 12. Effect of slenderness ratio on the axial load-axial displacement behavior of the specimens

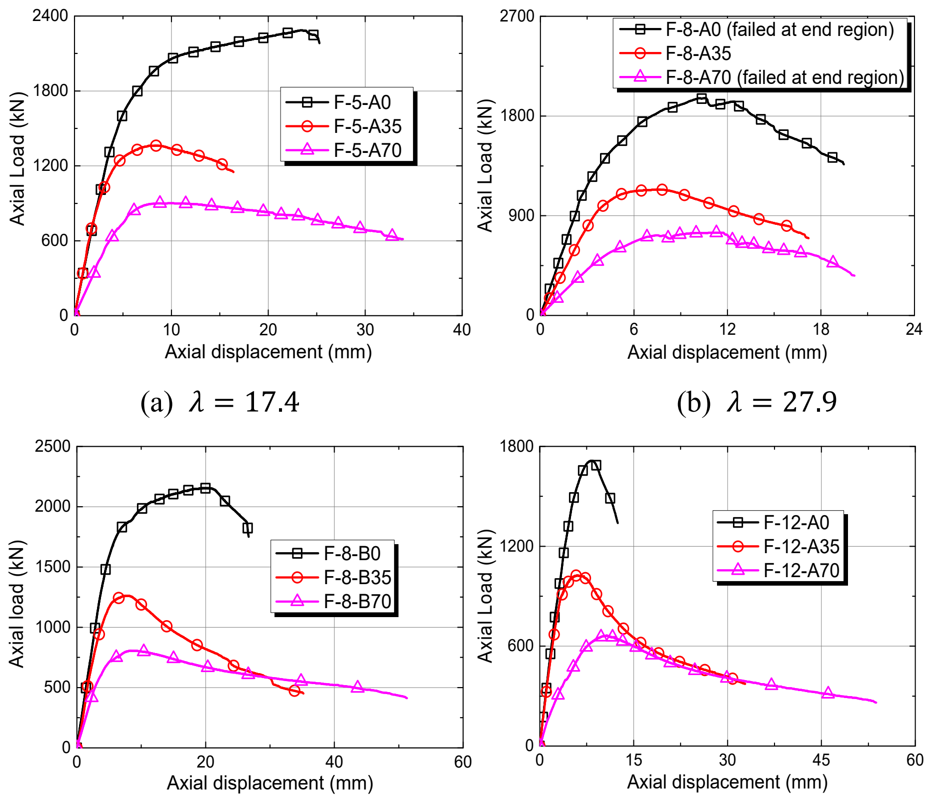

(a) $\lambda = 17.4$ (b) $\lambda = 27.9$

(c) $\lambda = 27.9$ (d) $\lambda = 41.8$

Figure 13. Effect of load eccentricity on the axial load-axial displacement behavior of specimens

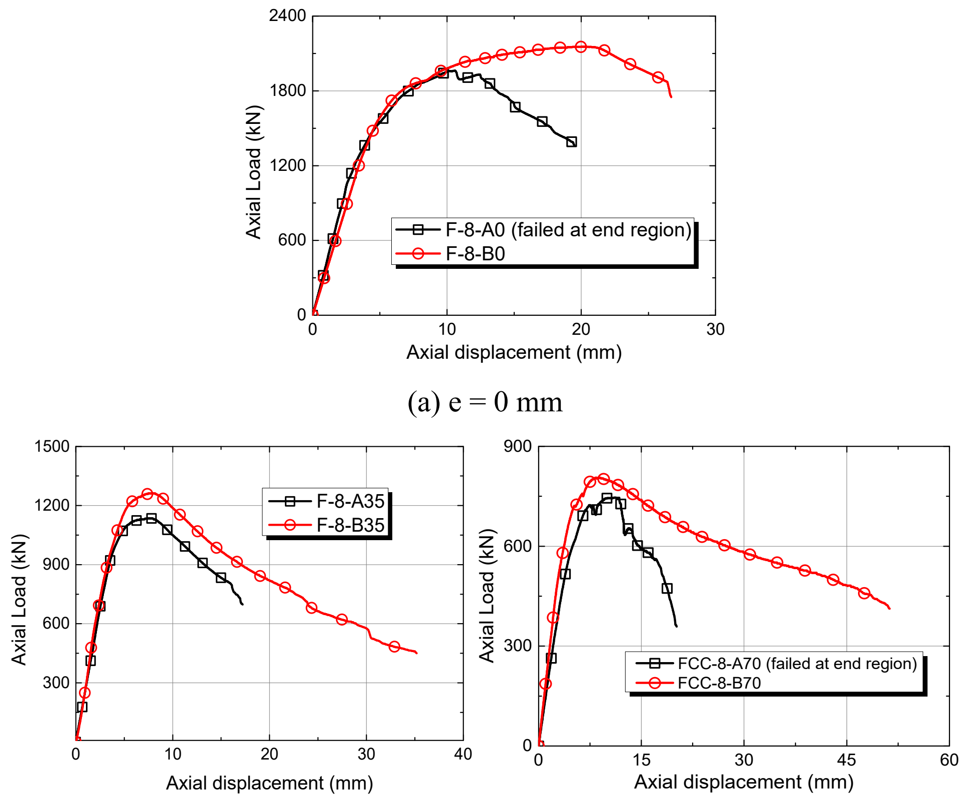

(a) e = 0 mm

(b) e = 35 mm

(c) e = 70 mm

Figure 14. Effect of FRP tube thickness on the axial load-axial displacement behavior of specimens

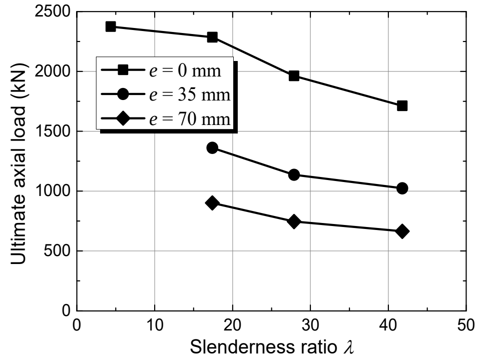

Figure 15. Effect of slenderness ratio on the ultimate axial load of specimens (with thin FRP tube)

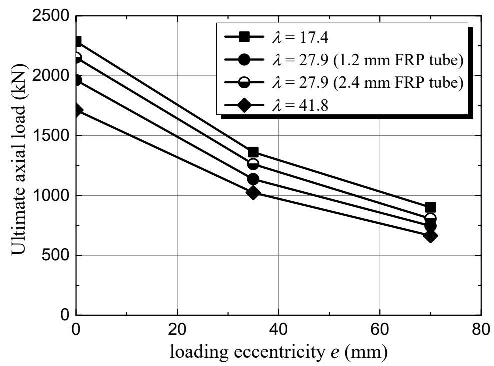

Figure 16. Effect of load eccentricity on the ultimate axial load of the specimens

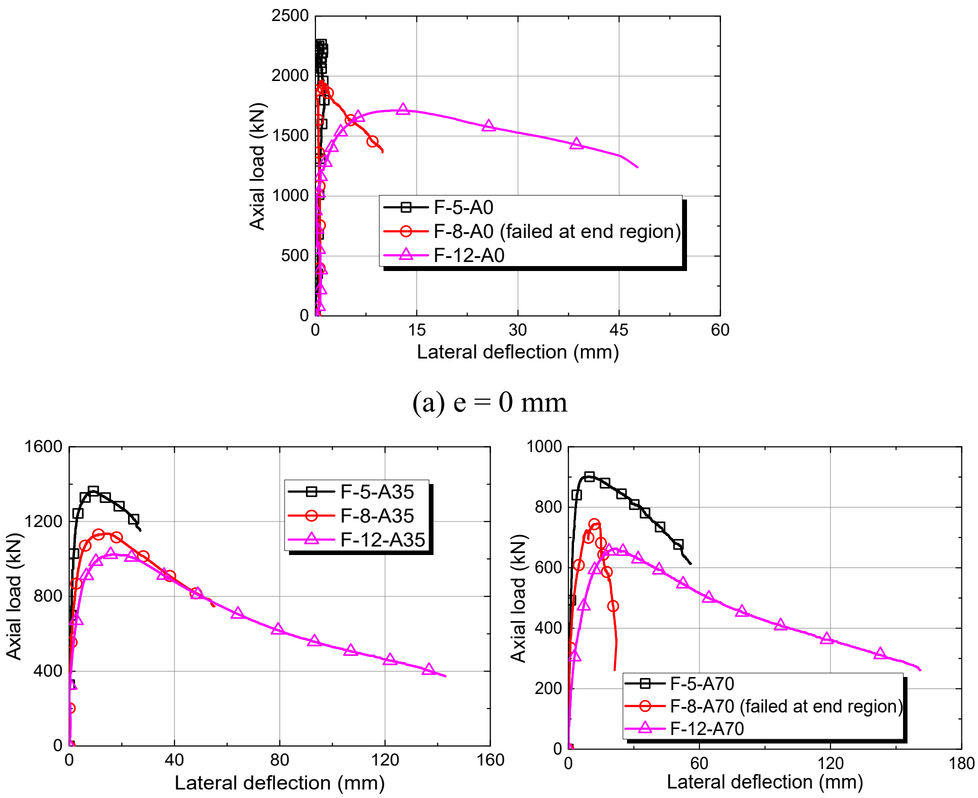

(a) e = 0 mm

(b) e =35 mm

(c) e = 70 mm

Figure 17. Effect of slenderness ratio on the axial load-lateral deflection curves of the specimens

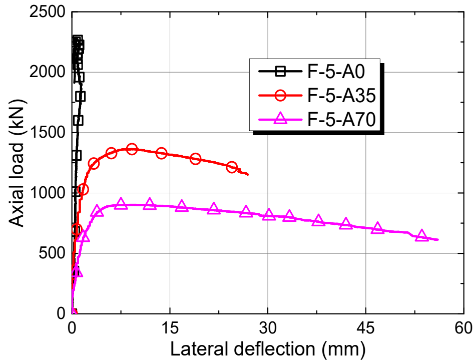

(a) $\lambda = 17.4$

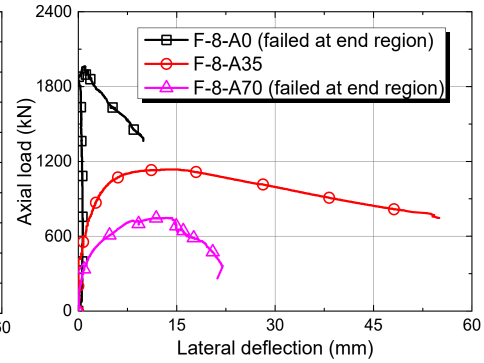

(b) $\lambda = 27.9$

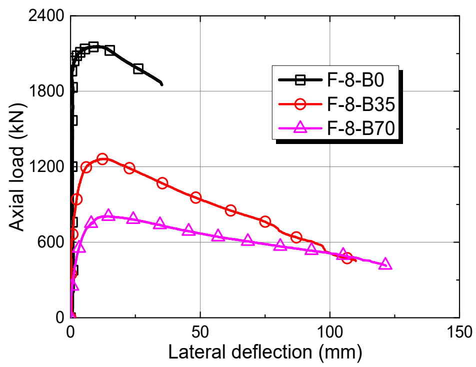

(c) $\lambda = 27.9$

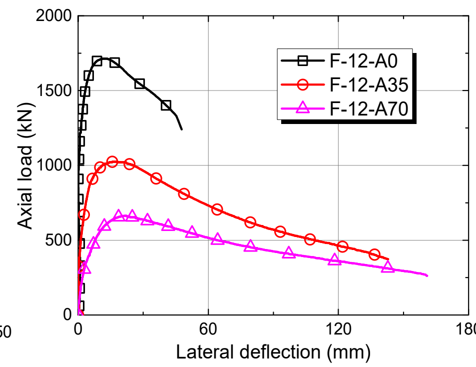

(d) $\lambda = 41.8$

Figure 18. Effect of load eccentricity on the axial load-lateral deflection curves of the specimens

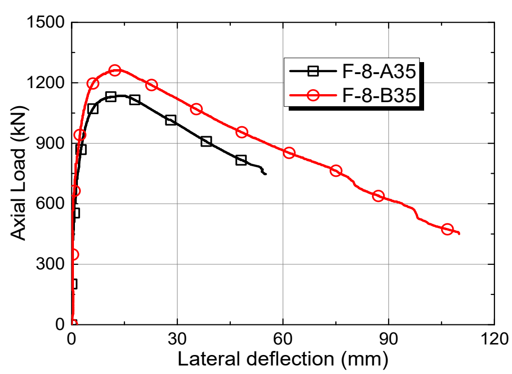

(a) e=35 mm

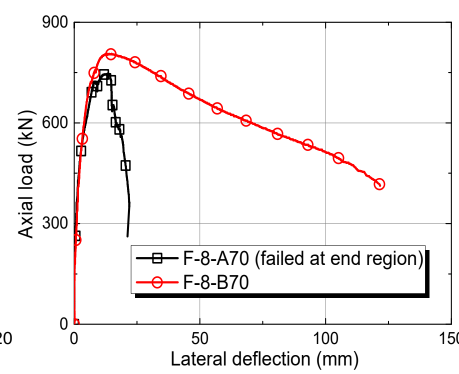

(b) e=70 mm

Figure 19. Effect of FRP tube thickness on the axial load-lateral deflection curves of the specimens

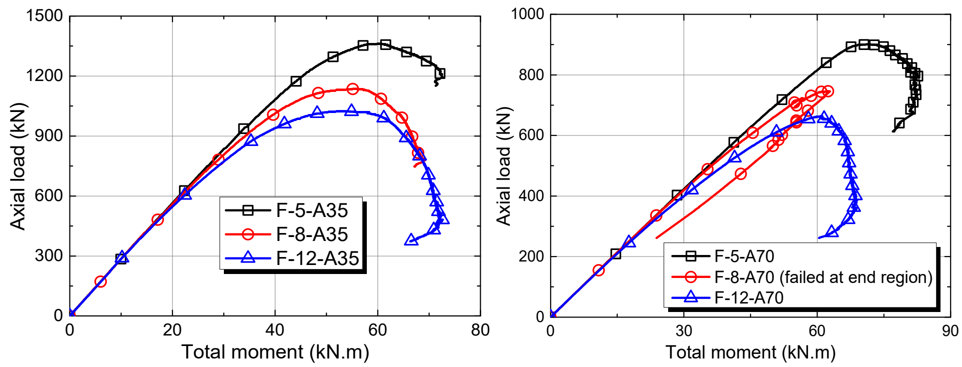

(a) (b)

Figure 20. Effect of slenderness ratio on axial load-moment curves.

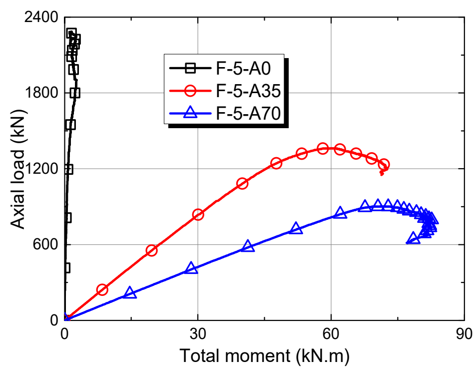

(a)

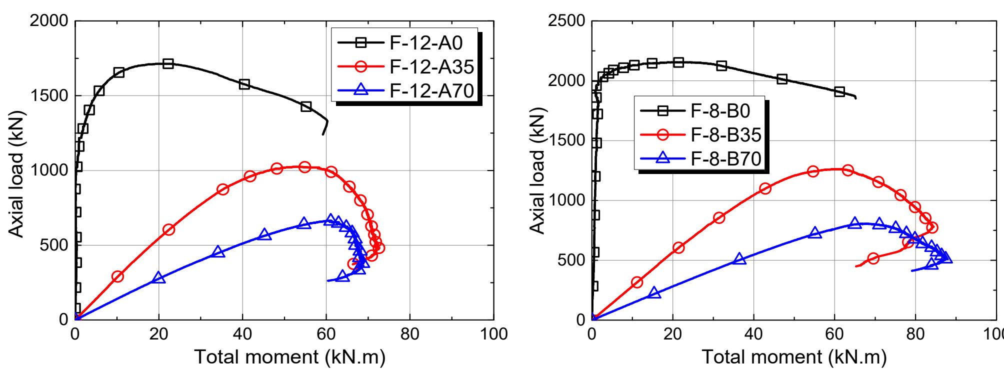

(b) (c)

Figure 21. Effect of load eccentricity on axial load-moment curves

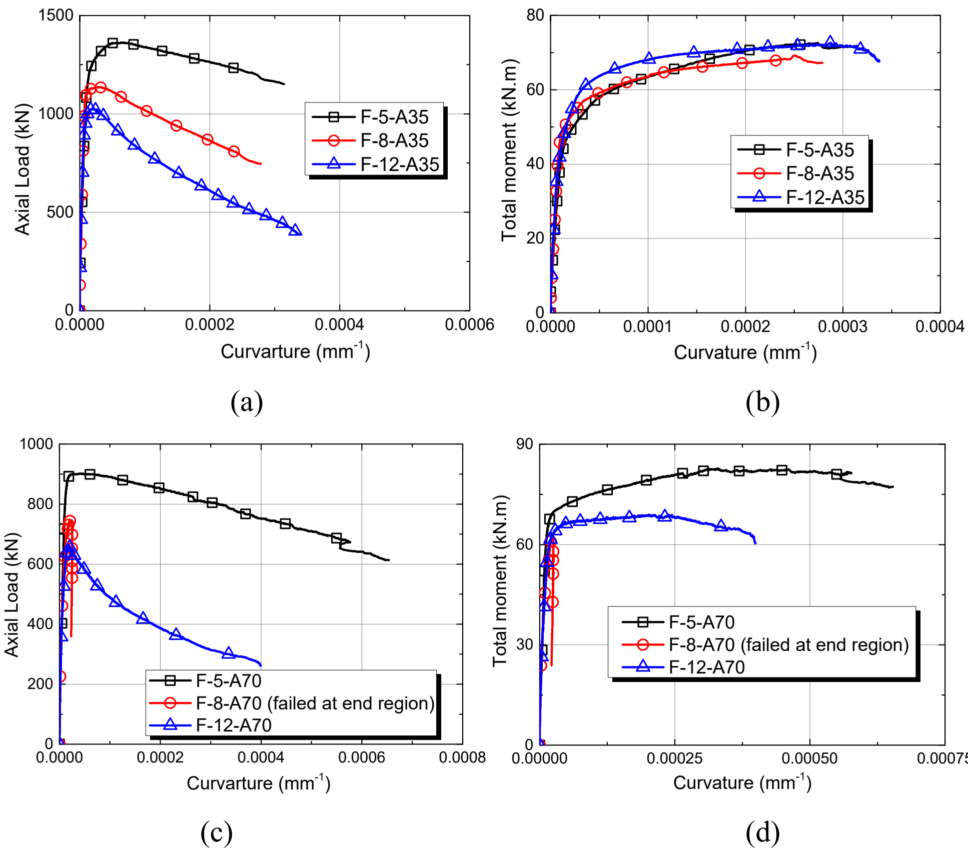

Figure 22. Effect of slenderness ratio on the axial load-curvature curve and moment-curvature curve of FCCSCs.

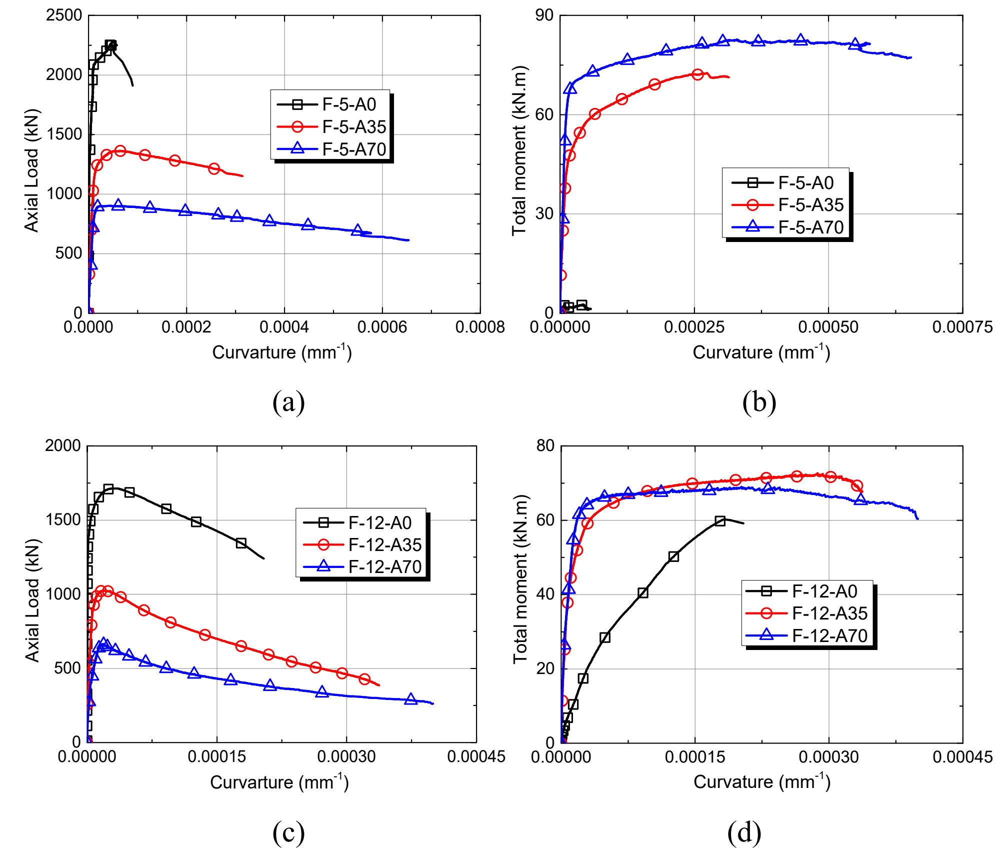

Figure 23. Effect of load eccentricity on the axial load-curvature curve and moment-curvature curve of FCCSCs.

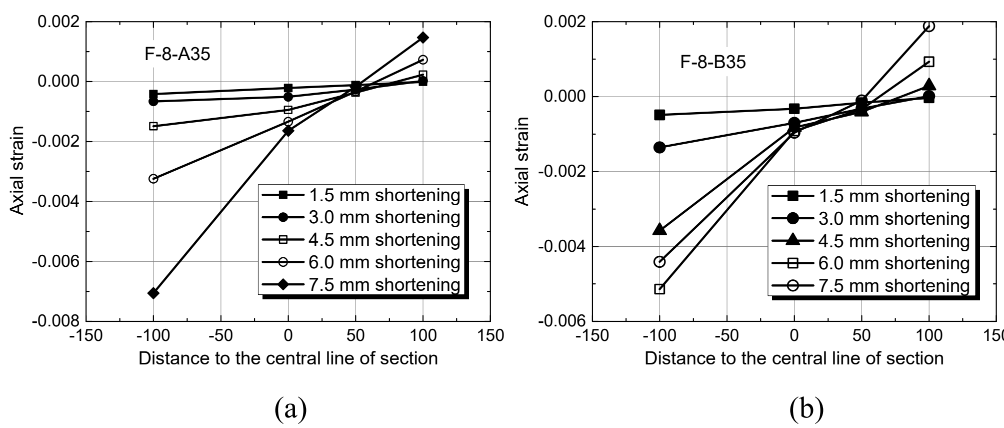

Figure 24. Distribution of axial strains over the cross section of the steel sections in FCCSCs: (a) F-8-A35; (b) F-8-B35

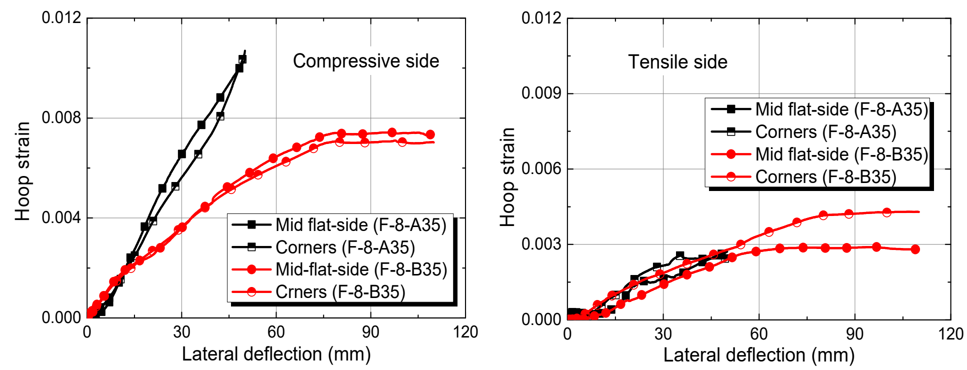

(a) (b)

Figure 25. Effect of FRP tube thickness on the hoop strain behavior of the FRP tube at the mid-height section

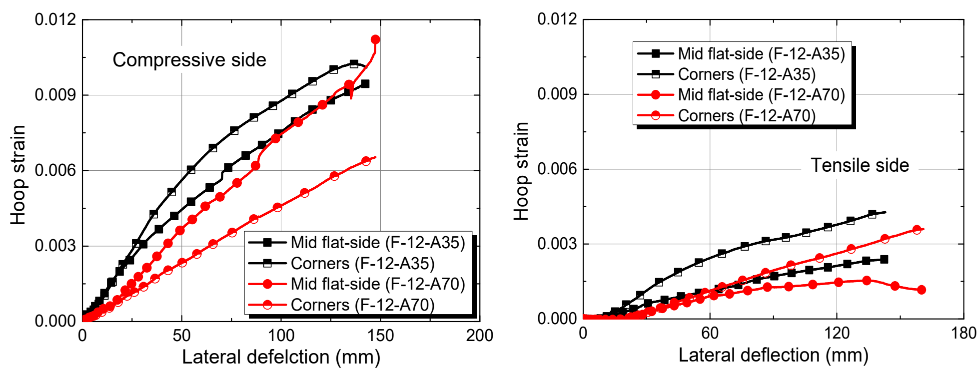

(a) (b)

Figure 26. Effect of load eccentricity on the hoop strain behavior of the FRP tube at the mid-height section

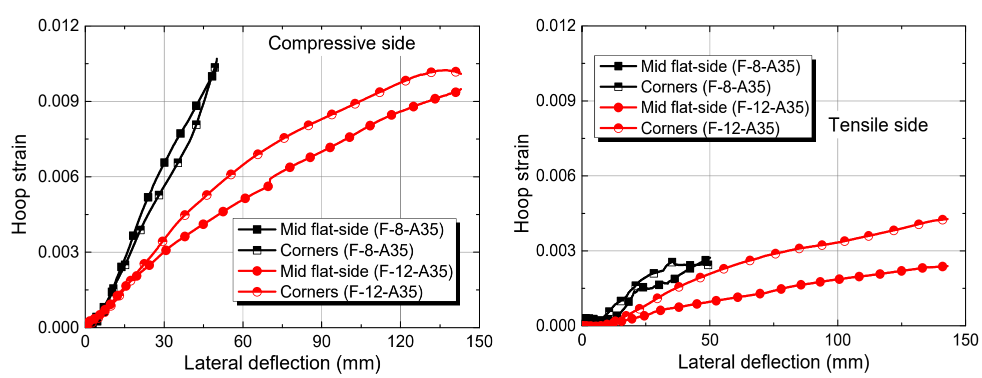

(a) (b)

Figure 27. Effect of slenderness ratio on the hoop strain behavior of the FRP tube at the mid-height section